

Magnetic anisotropy of CeCoSi under high magnetic field

T. Kanda ^{1,*}, H. Ishikawa ¹, S. Imajo ¹, K. Kindo,¹ H. Tanida ², and Y. Kohama ¹

¹*Institute for Solid State Physics, University of Tokyo, Kashiwa, Chiba 277-8581, Japan*

²*Liberal Arts and Sciences, Toyama Prefectural University, Imizu, Toyama 939-0398, Japan*



(Received 6 November 2023; revised 10 March 2024; accepted 19 March 2024; published 2 May 2024)

We have investigated the high magnetic field properties of the Ce-based Kondo lattice system CeCoSi by means of magnetization, magnetocaloric effect, contactless resistivity, specific heat, and magnetic torque measurements under pulsed high magnetic fields up to 55 T. CeCoSi is proposed to show an unconventional ordered phase called Phase II, which appears between paramagnetic Phase I and antiferromagnetic Phase III. The magnetization, magnetocaloric effect, and contactless resistivity measurements determine the field-angle dependence of Phase II-III boundary. Magnetic torque measurements detect a fourfold symmetry of the magnetic anisotropy under high magnetic fields in all phases, implying that there are two magnetic hard axes in the (100) or (110) plane of the tetragonal structure. Through comparison between the mean-field calculation and magnetization data, we determine the crystal electric field energy scheme, which agrees with the previous inelastic neutron scattering experiment. We successfully reproduce the fourfold magnetic anisotropy through our calculation, which is attributed to hybridization of the crystal electric field wave functions. The hybridization increases multipole degrees of freedom and is the origin of the unconventional order in Phase II. Moreover, the specific heat below 4 K exhibits a nonphononic T^3 term in Phase II, which indicates that Phase II is not a simple polarized paramagnetic state and can be a quadrupolar ordered state.

DOI: [10.1103/PhysRevB.109.174402](https://doi.org/10.1103/PhysRevB.109.174402)

I. INTRODUCTION

Kondo lattice system, which hosts the strong spin-orbit interaction and c - f hybridization, offers a rich playground to search for remarkable physical phenomena. In particular, a long-ranged order called “hidden order” (HO), whose order parameter (OP) is not identified, is one of the lively discussed topics in f -electron systems, including the most enigmatic HO of URu₂Si₂ [1,2].

When the crystal electric field (CEF) ground state possesses multipole degrees of freedom, electric and magnetic multipoles are expected to be possible OPs for the HO states, e.g., antiferroquadrupolar (AFQ) and magnetic octupolar orderings of Ce_{1-x}La_xB₆ [3–5], PrPb₃ [6–8], PrT₂Zn₂₀ ($T = \text{Ir, Rh}$) [9–12], ferroquadrupolar order of PrTi₂Al₂₀ [13–15]. Recent theoretical studies stimulate further studies on multipolar orderings in the Kondo lattice system along with the proposal of novel types of multipoles, known as odd-parity multipoles [16,17]. Orderings of odd-parity multipoles break spatial inversion symmetry and induce cross-correlated phenomena [18]. A notable example is the magnetic toroidal ordering observed in UNi₄B, which is one of the odd-parity multipolar orderings. This compound exhibits the current-induced magnetization [19].

CeCoSi belongs to the Ce-based Kondo lattice system and crystallizes in the tetragonal structure with a space group of $P4/nmm$ [20]. The spatial inversion symmetry is locally broken at the Ce site in this crystal. Under zero magnetic

field and ambient pressure, CeCoSi shows an unconventional ordered phase at $T_0 \sim 13$ K and an antiferromagnetic (AFM) order at $T_N = 9.4$ K. The unconventional phase was initially reported in a polycrystalline sample under high pressure [21] and a subsequent single-crystal study revealed that the novel phase persists even at ambient pressure [20]. This ordered phase was proposed to be a HO phase and named Phase II, as located between Phase I (paramagnetic phase) and Phase III (AFM phase), as shown in Fig. 1. The suppression of Phase II by La substitution suggests that the Ce $4f$ electron is a plausible origin of Phase II [22]. Unlike the case of the AFM transition, the transition temperature T_0 increases with applying magnetic fields, which is reminiscent of the AFQ ordered phase in CeB₆ [3]. However, the CEF ground state (GS) of CeCoSi is a Kramers doublet because of its tetragonal structure. A Kramers doublet does not have multipole degrees of freedom and quadrupolar orderings are basically impossible.

Recent investigations mainly explore the OP of Phase II. Theoretical studies discussed odd-parity multipolar orderings and the concomitant cross-correlated phenomena, with a focus on the locally broken spatial inversion symmetry [23,24]. It was subsequently suggested that the $(3z^2 - r^2)$ -type AFQ interaction assists interorbital quadrupolar orderings in the tetragonal symmetry [25]. On the experimental side, the nuclear magnetic resonance (NMR) and nuclear quadrupole resonance (NQR) experiments suggested the AFQ or higher-rank multipolar ordered state [26]. While the NMR and NQR experiments could not find any reduction of the local symmetry on the Co site, the x-ray diffraction (XRD) experiment reported a triclinic lattice distortion at T_0 [27]. Moreover, the XRD and recent comprehensive

*t.kanda@issp.u-tokyo.ac.jp

studies proposed the emergence of another field-induced phase [28], which suggested that the OP of Phase II might change by applying magnetic fields. More recently, detailed NMR measurements were performed [29]. By taking into account the triclinic lattice distortion reported in the XRD experiment, the latest NMR study suggested the zx -type ferroic quadrupolar order in the lower field phase of Phase II.

Despite these intensive efforts, the OP of Phase II has not been well understood. One reason is robustness of Phase III under magnetic fields. The magnetization measurement on polycrystalline samples indicates that Phase III persists even in high magnetic fields of up to ~ 20 T at 1.5 K [20], which prevents experimental investigations of Phase II at low temperatures. Another reason is the difficulty in determining the CEF energy diagram. By means of the specific heat measurement, Mitsumoto *et al.* first reported an energy diagram consisting of the Γ_7 ground state (GS), the Γ_6 first excited state and the Γ_7 second excited state (i.e., Γ_7 - Γ_6 - Γ_7), and the energy gap between the GS and the first (second) excited states was determined to be 90 K (208 K) [30]. However, Γ_7 - Γ_7 - Γ_6 with the energy gaps between the GS and the first (second) excited states of 125 K (165 K) were reported by the inelastic neutron scattering and specific heat measurements [31]. This inconsistency poses a significant challenge to our understanding of the OP because the multipole degrees of freedom are linked to the CEF wave functions. Even though quantitative magnetization analysis provided the CEF parameters in other Kondo lattice systems $R\text{CoGe}_3$ ($R = \text{Ce}, \text{Pr}, \text{Nd}$) [32,33], CeIrSi_3 [34], $\text{CeT}_2\text{Al}_{10}$ ($T = \text{Fe}, \text{Ru}$) [35,36], and PrPb_3 [6], there have been no magnetization measurements on CeCoSi with a single-crystalline sample above 7 T.

In this research, we have investigated the high field properties of CeCoSi in magnetic fields up to 55 T to unveil the detailed properties of Phase II. We carried out the magnetization, magnetocaloric effect (MCE), contactless resistivity, specific heat, and magnetic torque measurements. Experimental details of these measurements are described in Sec. II. Experimental results with the magnetic field-angle phase diagram obtained in this study are presented in Sec. III. In Sec. IV A, we perform the two-sublattice mean-field self-consistent calculation and fit the experimentally obtained magnetization and magnetic susceptibility data. The magnetic anisotropy is calculated in Sec. IV B, and the CEF energy scheme is numerically obtained in Sec. IV C. We discuss the magnetization and magnetic anisotropy based on the obtained CEF scheme in Sec. V A. The implications of high-field C_p data are presented in Sec. V B.

II. METHODS

Single crystals of CeCoSi were prepared by a Ce/Co eutectic flux method [20]. Magnetization measurements were performed by the induction method up to around 55 T in pulsed magnetic fields, where the field directions were along the [001] and [100] axes. The pulsed field data were calibrated by the magnetization data up to 7 T obtained by a commercial SQUID magnetometer (MPMS, Quantum Design). Magnetic torque was measured using a commercial piezoresistive cantilever (SEIKO PRC-120) [37]. In the magnetic torque measurements, the direction of the magnetic field was

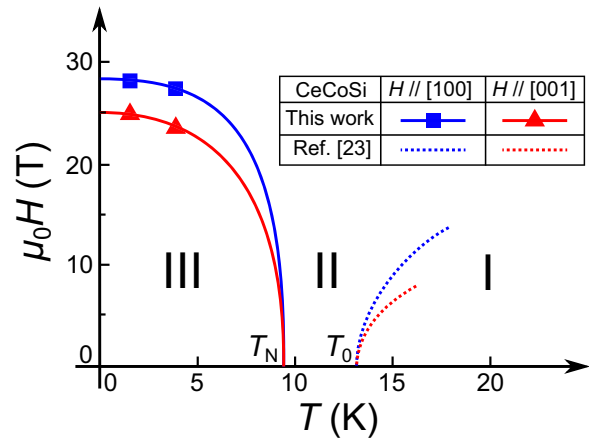


FIG. 1. H - T Phase diagram of CeCoSi . The blue and red lines correspond to $H // [100]$ and $H // [001]$, respectively. The phase boundaries between Phase II and Phase III, plotted by solid lines, are obtained in this paper. The dotted lines indicate the boundary between Phase I and Phase II, cited from Ref. [28].

rotated using a plastic single-axis rotator. The relative change in magnetic torque was obtained by measuring the corresponding change in resistivity of the piezoelectric cantilever. The magnetic field was rotated from the [001] axis to the (001) plane, where the azimuthal orientation could not be determined owing to the small sample size of less than 0.1 mm. For the radio-frequency noncontact resistivity measurement [38], the sample was placed within one of double counter-wound pick-up coils of 0.5 mm diameter, which could cancel out the voltage induced by rapid field sweeps of pulsed magnetic fields. The resonant circuit incorporated with a tunnel diode oscillator (TDO) was driven with a resonance frequency of ~ 80 MHz. In this paper, we abbreviate this method to the TDO measurement. The sample was placed on the single-axis rotator to change the field direction in the same manner as the magnetic torque measurements. The direction of the magnetic fields was rotated within the (010) plane. Measurements of specific heat were performed by the quasi-adiabatic method [39,40] in highly stabilized magnetic fields generated by a long-pulse magnet [41,42]. Magnetocaloric effect (MCE) measurements on the same single crystal were performed by the same calorimeter under quasi-adiabatic conditions. For the specific heat and MCE measurements, the magnetic fields were applied along the [001] axis of the sample.

III. RESULTS

A. Magnetization

Figure 2 shows the magnetization curves obtained at temperatures of $T = 1.5, 4.2,$ and 30 K under pulsed magnetic fields. The magnetization data with applying magnetic fields along two crystallographic axes, $H // [100]$ and $H // [001]$, are shown in the upper and lower panels of Fig. 2, respectively. The magnetization curves below 4.2 K show a shoulder-like anomaly, which is attributed to the phase transition from Phase III to Phase II. We define the critical field B_c as the field where the anomaly is observed. B_c slightly varies depending on the field direction; $B_c = 28$ T for $H // [100]$ and

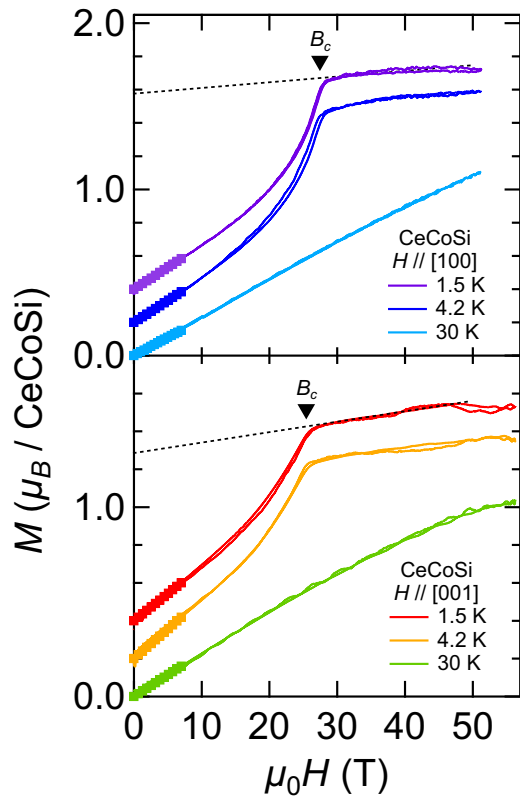


FIG. 2. Magnetization curves of CeCoSi single crystal at $T = 1.5, 4.2,$ and 30 K. The magnetization data in the upper and lower figures were taken by applying the magnetic fields parallel to the $[100]$ and $[001]$ axes, respectively. The square symbols show the magnetization data obtained by the SQUID magnetometer. The magnetization data at $T = 4.2$ and 1.5 K are shifted with offsets of $0.2 \mu_B$ and $0.4 \mu_B$ for clarity. The black triangular markers indicate the critical fields (B_c). The dotted lines are the guides to the eye.

$B_c = 25$ T for $H//[001]$. There are no significant differences in B_c at 4.2 K and 1.5 K for both field directions. The slope of the magnetization curves becomes steeper just below B_c . The origin of the concave-shaped curves is discussed in Sec. V A. For $H//[100]$, there is a small open loop on the concave-shaped curve below B_c at 4.2 K. This loop might come from MCE. Namely, the hysteretic temperature change due to MCE leads to different magnetization values in up- and down-sweep processes. The hysteretic behavior is also observed above B_c at 1.5 K. The hysteresis might relate to open loops observed in torque magnetometry as discussed later. The magnetization data for $H//[001]$ show a saturation tendency with a slight slope up to 55 T. We also observe hysteresis below 4.2 K for this field direction. These hysteresis might appear due to poor signal-noise ratio. We estimate the size of the magnetic moments saturated above B_c by the linear extrapolations of the magnetization curves between 30 and 40 T. The estimated moment sizes are $1.2 \mu_B$ for $H//[100]$ and $0.9 \mu_B$ for $H//[001]$.

On the other hand, the magnetization curves at 30 K show no distinctive features regardless of field directions. The magnetic anisotropy is negligibly small below 20 T, while the magnetization for $H//[100]$ is larger than that for $H//[001]$ above 20 T. If the transition temperature from Phase I to Phase

II monotonically increases as reported in low-field region [20,28], the transition is expected to occur at 30 K and 40 T for $H//[100]$ and $H//[001]$ due to the reentrant behavior of Phase II. One possibility of the absence of the anomaly is that the increase of Phase I-II boundary temperature is suppressed at high magnetic fields. Namely, the measurement temperature of 30 K is too high, and/or the field strength of 55 T is too low to induce the transition between Phase I and Phase II. The other possibility is that the anomaly at the phase boundary is tiny and hardly detectable in our experiment. In fact, this anomaly is barely observable even in steady field experiments [20,28]. Our measurements performed in pulsed magnetic fields are less sensitive than those performed in steady fields, and the resolution may not be sufficient to detect the subtle field-induced anomaly.

B. Magnetic torque

Figures 3(a) and 3(b) show the field dependencies of the magnetic torque at 1.5 K and 30 K. The field angle shown in the left axis of Figs. 3(a) and 3(b) corresponds to the polar angle θ' between the fields and the $[001]$ axis, where the azimuthal angle is not known. The magnetic field lies on the ab plane at $\theta' = 90^\circ$. At 1.5 K, the magnetic torque shows huge hysteresis when $\theta' = 90^\circ$. We will discuss this hysteresis in Sec. V A. Regardless of the measurement temperature, the amplitude of the torque monotonically decreases with rotating the field angle from 0° to 45° and from 90° to 135° , while it increases with the angle from 45° to 90° . This indicates the sign reversal of the torque signal at every 45° . This behavior can be clearly seen in the angle dependence of torque at several magnetic fields [Fig. 3(c)]. In general, when the magnetic field rotates in the (100) plane, the torque obeys $\tau \propto \sin 2\theta'$ [43–48]. Therefore, the torque is expected to show the reversal of the sign at every 90° , which yields twofold behavior. However, our magnetic torque data reverses its sign every 45° , which is called fourfold behavior. As seen in Fig. 3(c), the fourfold behavior is observed above 15 T. The angles at which the sign of the torque is reversed are independent of the field strength. Figure 3(d) shows the angle dependence of the magnetic torque obtained at 20 T and at various temperatures. This supports that the reversal of the torque signal is observed not only in Phase I (30 K) but also in Phase II (10.5 K) and Phase III (1.5 K), indicating that the unique magnetic anisotropy exists regardless of its ordered states.

C. TDO, MCE, and phase diagram

Figure 4(a) shows the field dependence of TDO frequency at 1.5 K. The field was applied in the (010) plane with changing the polar angle θ between the magnetic fields and the $[001]$ axis, i.e., the field is along the $[100]$ axis when $\theta = 90^\circ$. In the TDO measurement, the change in the frequency mostly relates to the change in resistivity [38]. As shown in the field derivative of the TDO frequency in Fig. 4(b), the anomalies indicated by the markers are clearly observed as peak structures in the field range between 23 and 30 T. The peak positions at $\theta = 0^\circ$ and 90° are consistent with those of the phase transition field observed in the magnetization, and thus

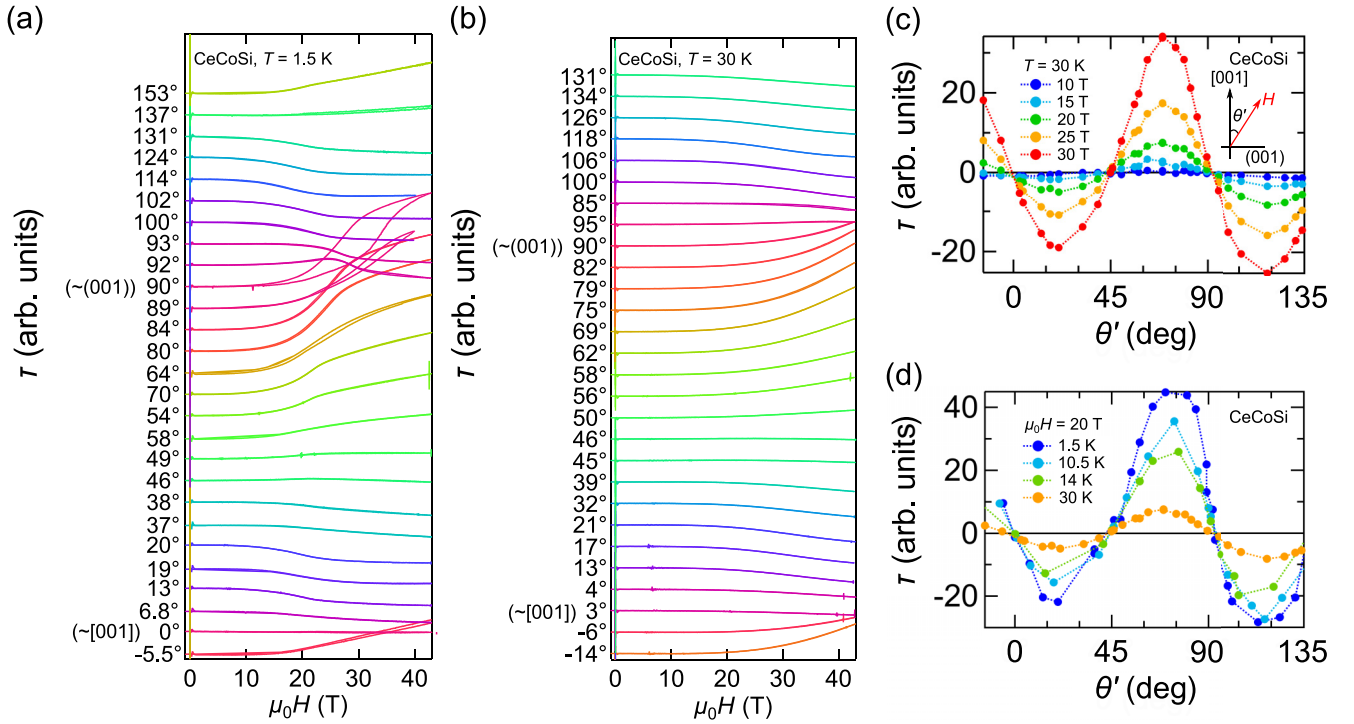


FIG. 3. (a), (b) Field dependence of magnetic torque for various field directions. (a) and (b) correspond to the data taken at 1.5 K and 30 K, respectively. (c) Angle dependencies of magnetic torque at a temperature of 30 K. The blue, cyan, green, orange, and red markers correspond to the fields of 10, 15, 20, 25, and 30 T, respectively. (d) Angle dependencies of magnetic torque at fixed magnetic fields of 20 T. The blue, cyan, green, and orange markers correspond to the temperature of 1.5, 10.5, 14, and 30 K, respectively.

we deduce the angle dependence of the critical fields B_c with the angle-dependent TDO data. We note that the oscillatory behavior observed in Fig. 4(b) is not caused by quantum oscillations.

Figure 4(c) shows the MCE curves taken with the field parallel to the $[001]$ axis. In general, MCE is induced by the field dependence of magnetic entropy, which leads to a change in the sample temperature as a function of the magnetic field. When the entropy changes at a phase boundary, a kink appears in MCE curves [49], typically indicating a phase transition. As pointed by the markers in Fig. 4(c), the kink structures are observed below 4 K. The kink position observed with the MCE curve shows a good agreement with the B_c obtained by the magnetization measurements in Fig. 2. On the other hand, no anomaly is observed around 15 K, where the phase transition from Phase I to Phase II was reported to occur [20,28]. This should result from a small entropy change across Phase I-II boundary. In fact, the anomaly corresponding to the phase transition is tiny in the specific heat measurements [28], which indicates a small entropy change in the phase boundary.

Figure 4(d) shows the magnetic field-angle phase diagram between Phase III and Phase II determined by the magnetization, MCE, and TDO experiments. Our phase diagram clearly shows that the B_c has two maxima at $\theta \simeq 0^\circ$ and 80° . The former corresponds to the field alignment of $H//[001]$. The latter one is slightly deviated from the $[100]$ axis, which might be due to the lack of measurement resolution. Since the saturation fields are considered to have the maximum value by applying the magnetic field along the magnetic hard axis, our results imply that both the $\sim[001]$ and $\sim[100]$ axes are the

hard axes. Such a double-maximum structure is not common, because the hard axis is typically either the $[001]$ axis or on the (001) plane in tetragonal magnetic compounds [45,46]. Later in Sec. IV B, we reveal that the CEF effect on the f electrons gives rise to the field-induced hard axis along the $[001]$ axis in addition to the zero field one in the (001) plane. It is worth noting that the direction of magnetic moments in Phase III slightly tilts from the $[100]$ axis and points to $\theta \simeq 80^\circ$ [26], which might relate to the deviation of the maximum from the $[100]$ axis in the angle phase diagram.

D. Specific heat

Figure 5(a) shows the temperature dependence of the specific heat C_p in CeCoSi at 0, 16.2, 21.6, and 27.4 T. The C_p data at 0 T show a λ -type anomaly at 9.4 K and a small bump at around 13 K. These anomalies correspond to T_N and T_0 , which are consistent with the previous reports [20,28]. At 21.6 T, the peak at T_N shifts to 5.3 K due to the suppression of Phase III. To extract the anomalous contribution to the specific heat (C_{ano}) from total specific heat, we subtract the phonon contribution as $C_{\text{ano}} = C_p - C_{\text{lattice}}$, where the phonon contribution, $C_{\text{lattice}} = 0.30T^3$ mJK $^{-1}$ mol $^{-1}$, of the nonmagnetic LaCoSi is used [20]. As shown in the dotted curve in Fig. 5(a) and its inset, C_{lattice} is about two orders of magnitude smaller than the C_p at 1.2 K and is almost negligible. Figure 5(b) is the C_{ano}/T versus T^2 plot below 2 K. Since the plots fall on straight lines with finite intercepts, C_{ano} is expressed by the combination of the linear (γT) and cubic (bT^3) terms as

$$C_{\text{ano}}/T = \gamma + bT^2. \quad (1)$$

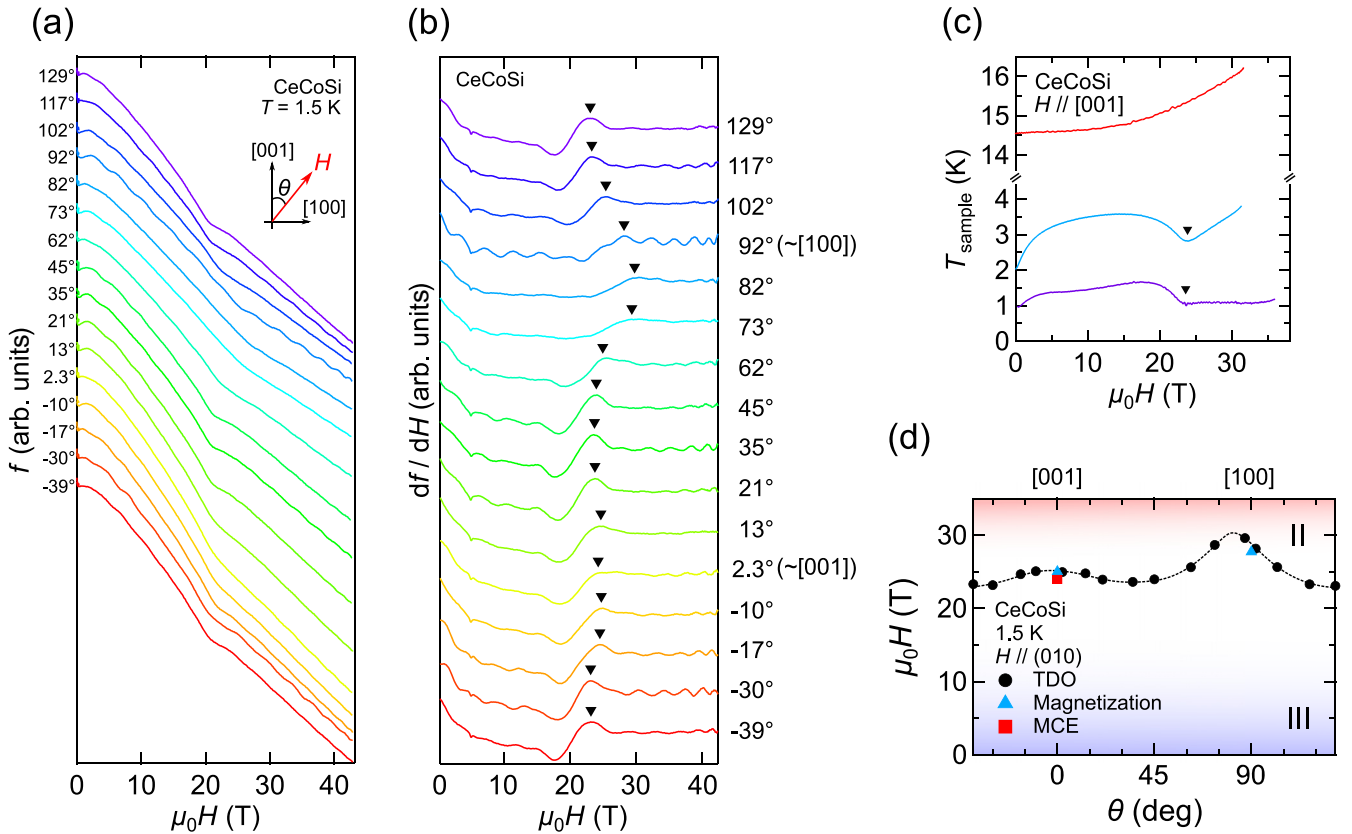


FIG. 4. (a) Field dependence of TDO frequency at 1.5 K taken in the field decreasing process. The field is in the (010) plane and the field angle θ is the polar angle between the magnetic fields and the [001] axis. (b) Derivation of the TDO frequency in (a). The markers indicate the critical fields B_c . (c) MCE curves in the field-decreasing process. The magnetic fields were applied parallel to the [001] axis. The results with three different initial sample temperatures of 1.0, 2.0, and 14.5 K are shown. The markers indicate the critical fields B_c . (d) Magnetic field-angle phase diagram. The magnetic fields are rotated in the (010) plane. The round, triangle, and rectangle markers correspond to the critical field observed by the TDO, the magnetization, and MCE, respectively. The lower blue region indicates Phase III while the upper red region shows Phase II. The dotted line is the guide for the eye.

The coefficient of the linear term γ corresponds to the intercept of the C_{ano}/T versus T^2 plot, which is proportional to the electronic density of states. The observed γ is about

$20 \text{ mJK}^{-2}\text{mol}^{-1}$ at zero field, which is consistent with previous report [20]. It is important that γ of CeCoSi is almost the same as that of LaCoSi, $18 \text{ mJK}^{-2}\text{mol}^{-1}$ [20], indicating the

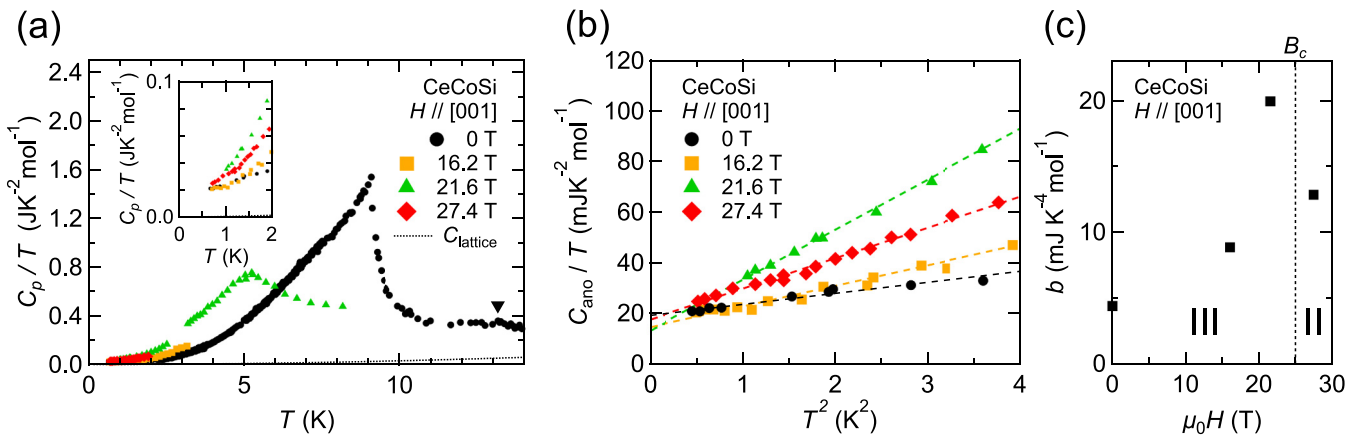


FIG. 5. (a) Temperature dependence of C_p/T for $H//[001]$. The black, orange, green, and red symbols correspond to datasets of $\mu_0H = 0, 16.2, 21.6, 27.4 \text{ T}$, respectively. The dashed line shows C_{lattice} , i.e., the specific heat of LaCoSi [20]. The black triangle marker represents the anomaly at $T_0 \sim 13 \text{ K}$. The inset represents C_p/T data below 2 K. (b) Anomalous contribution of the specific heat C_{ano} plotted as C_{ano}/T vs T^2 . C_{ano} is obtained by subtracting the lattice specific heat of LaCoSi reported in Ref. [20] from our C_p data. The dotted lines are the linear fit to the respective datasets at low temperatures. (c) Field dependence of T -cubic coefficient b . The dotted line corresponds to the critical field.

weak c - f hybridization in this system. In fact, the observed γ is independent of the field strength up to 27.4 T, which supports that the $4f$ electrons are almost localized. While γ does not change across the critical fields, the coefficient b , i.e., the slope of the plot, strongly depends on the field strength. Since the lattice contribution is already subtracted in C_{ano} , the origin of b at zero magnetic fields can be interpreted as the Goldstone mode, i.e., the antiferromagnetic magnon excitation. The diverging behavior of b below B_c [Fig. 5(c)] might relate to the reduction of T_N as the field increases [50]. At 27.4 T, the b of $12 \text{ mJK}^{-4} \text{ mol}^{-1}$ is 2.8 times larger than that at 0 T despite of suppression of the AFM order. We will make a detailed discussion about the anomalous power-law behavior in Sec. V B and propose that the anomalous T^3 term originates from the unconventional OP of Phase II.

IV. MEAN-FIELD CALCULATION

A. Two-sublattice model and data fit

To obtain the CEF parameters and investigate the origin of the unique magnetic anisotropy observed in the magnetic torque and phase diagram, we perform the two-sublattice mean-field calculation. The Hamiltonian \mathcal{H} for Cerium $4f^1$ electron is given by

$$\mathcal{H} = \mathcal{H}_{\text{CEF}} + \mathcal{H}_{\text{Zeeman}} + \mathcal{H}_{\text{Exchange}}, \quad (2)$$

$$\mathcal{H}_{\text{CEF}} = B_2^0 \hat{O}_2^0 + B_4^0 \hat{O}_4^0 + B_4^4 \hat{O}_4^4, \quad (3)$$

$$\mathcal{H}_{\text{Zeeman}} = -g_J \mu_B \hat{\mathbf{J}} \cdot \mu_0 \mathbf{H}, \quad (4)$$

$$\mathcal{H}_{\text{Exchange}} = J_{\text{ex}} \sum_{\langle rr' \rangle} \hat{\mathbf{J}}_r \cdot \hat{\mathbf{J}}_{r'}. \quad (5)$$

Here, B_2^0 , B_4^0 , and B_4^4 are the CEF parameters, \hat{O}_2^0 , \hat{O}_4^0 , and \hat{O}_4^4 are the Stevens's operators [51], $g_J = 6/7$ is the Landé's g factor, μ_B is the Bohr magneton, $\hat{\mathbf{J}} = (\hat{J}_x, \hat{J}_y, \hat{J}_z)$ is the total angular momentum operator, \mathbf{H} is the magnetic fields, and J_{ex} is the exchange constant. The symbol $\langle rr' \rangle$ denotes a sum over the nearest neighbors.

Since CeCoSi shows the antiferromagnetic transition, we take the two-sublattice model for this Hamiltonian. To make it solvable, we apply a mean-field approximation. Then we obtain the Hamiltonian on the sublattice A, B ,

$$\mathcal{H}(A) = \mathcal{H}_{\text{CEF}} + \mathcal{H}_{\text{MF}}(B), \quad (6a)$$

$$\mathcal{H}(B) = \mathcal{H}_{\text{CEF}} + \mathcal{H}_{\text{MF}}(A), \quad (6b)$$

where the mean field from the sublattice $R = A, B$ is defined as

$$\mathcal{H}_{\text{MF}}(R) = -g_J \mu_B \hat{\mathbf{J}} \cdot (\mu_0 \mathbf{H} + \tilde{\lambda} \langle \hat{\mathbf{M}} \rangle_R). \quad (7)$$

Here, $\tilde{\lambda}$ is the molecular fields. We set $\tilde{\lambda} = \text{diag}(\lambda_a, \lambda_a, \lambda_c)$ with taking the tetragonal structure into account. $\langle \hat{\mathbf{M}} \rangle_R = (\langle \hat{M}_x \rangle_R, \langle \hat{M}_y \rangle_R, \langle \hat{M}_z \rangle_R)$ is the thermal average of the magnetization on the sublattice R expressed as

$$\langle \hat{\mathbf{M}} \rangle_R = \sum_n \frac{\langle n, R | \hat{\mathbf{M}} | n, R \rangle}{Z} \exp\left(-\frac{E_{n,R}}{k_B T}\right), \quad (8)$$

TABLE I. Obtained CEF parameters and molecular field constants. Previously reported CEF parameters in Ref. [31] are also shown. In Ref. [31], the molecular fields are not taken into consideration, which is represented by “—”.

	B_2^0 (K)	B_4^0 (K)	B_4^4 (K)	λ_a (mol/emu)	λ_c (mol/emu)
This paper	-1.42	0.472	1.40	-14.0	-24.5
Ref. [31]	-1.26	0.487	1.35	—	—

where $E_{n,R}$, $|n, R\rangle$, and Z are the eigenenergy, the corresponding eigenstate of $\mathcal{H}(R)$, and the partition function, respectively.

We perform the self-consistent calculation for this model. The expected magnetization M is calculated as

$$M(\mathbf{H}) = \frac{\langle \hat{\mathbf{M}} \rangle_A + \langle \hat{\mathbf{M}} \rangle_B}{2} \cdot \frac{\mathbf{H}}{H}. \quad (9)$$

The inversed magnetic susceptibility $1/\chi$ is computed at a magnetic field of $\mu_0 H_0 = 1.0$ T,

$$\frac{1}{\chi} = \frac{1}{\chi_0} + \frac{H_0}{M(H_0)}. \quad (10)$$

Here, χ_0 is the temperature-independent magnetic susceptibility, which mainly originates from Pauli paramagnetism from Co ions.

We fit the experimental $M(\mathbf{H})$ curves taken at 30 K and $1/\chi(T)$ curves at 1.0 T to the calculated results, where B_2^0 , B_4^0 , B_4^4 , λ_a , and λ_c are the fitting parameters. Here, we subtract the magnetization of LaCoSi from the experimental data to omit magnetization from Co ion and χ_0 [20]. Table I summarizes the set of parameters used for the fits. Figure 6(a) shows the comparison between the calculated and the experimental $M(\mathbf{H})$ curves for both field angles of $H//[100]$ and $H//[001]$. Except for the slight deviation of fits above 40 T, both calculated curves agree with the experimental results. Figure 6(b) shows the experimental $1/\chi(T)$ data with the calculated results. Notably, the fitting curves successfully reproduce the temperature dependence of magnetic anisotropy. Besides, there are slight differences, less than 5%, between the calculated and experimental $1/\chi(T)$ curves for $H//[100]$ and $H//[001]$ at room temperature. These differences become negligible at ~ 80 K and reappear again at lower temperatures. We also calculated the Néel temperature by estimating the staggered magnetization $\langle \hat{\mathbf{M}} \rangle_A - \langle \hat{\mathbf{M}} \rangle_B$, which becomes nonzero for temperatures below T_N . This yields the Néel temperature of 11.5 K, which is close to the experimental value of $T_N = 9.4$ K.

While we successfully reproduce some magnetic properties, other physical properties derived from this model are inconsistent with the experimental results in addition to the deviation in the magnetization curves. For example, our model expects that the spin is parallel to the $[001]$ axis in Phase III. However, the inelastic neutron scattering and NMR experiments reported that the spin points to the $[100]$ axis [26,31]. Moreover, the size of magnetic moments is calculated to be $0.9 \mu_B/\text{Ce}$ by this model. Compared to the moment sizes estimated by our magnetization measurements, the calculated value is consistent for $H//[001]$ but inconsistent for

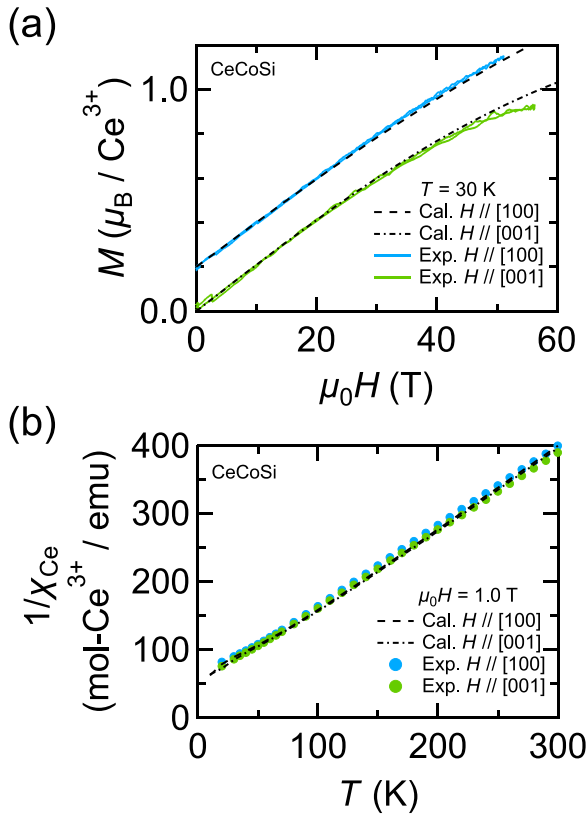


FIG. 6. (a) Calculated magnetization curves at 30 K. The black-dashed and dash-dotted lines correspond to the field parallel to the [100] and [001] axes, respectively. The blue and green solid lines are the magnetizations of Ce ion for $H//[100]$ and [001], in which the magnetization of Co ion is omitted from our experimental results by subtracting the magnetization of LaCoSi reported in Ref. [20]. The calculated and experimental results for $H//[100]$ are shown with an offset of $0.2 \mu_B$ for clarity. (b) Calculated inverse magnetic susceptibility at the field of 1.0 T. The color and line notations are the same as in (a). The experimental results are taken from Ref. [20].

$H//[100]$. These discrepancies should be attributed to interactions excluded in our model, e.g., electric quadrupole interactions and/or a triclinic lattice distortion reported by the XRD experiments [27].

B. Magnetic anisotropy

Figure 7 shows the polar plot of the calculated magnetization. The angular coordinate corresponds to the field angle from the [001] to the [100] axis [Fig. 7(a)] and to the [110] axis [Fig. 7(b)]. The radial coordinate is the magnetization normalized by its maximum value. In this plot, the magnetically hard (easy) axis corresponds to the direction where the magnetization is minimum (maximum). In Fig. 7(a), the 10-T data represented by the blue curve show an elliptical magnetization pattern, indicating the uniaxial magnetic anisotropy where the hard axis lies on the [100] axis. The direction of the hard axis is consistent with the low-field magnetic susceptibility data at 30 K [Fig. 6(b) [20]]. With increasing magnetic field to 20 T, the hard axis starts to emerge on the [001] axis. At $\mu_0H = 30$ T, the $M(\theta)$ exhibits a wasp-waist structure, characterized by four directions with

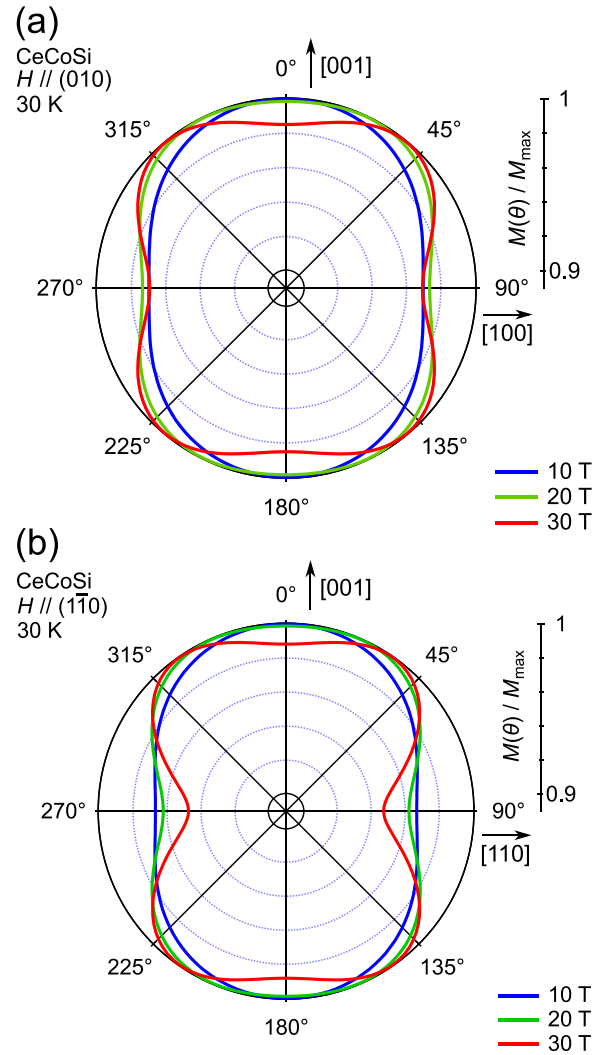


FIG. 7. Polar plot of the normalized magnetization of (a) $H//(010)$ and (b) $H//(\bar{1}\bar{1}0)$. The angular and radial coordinates correspond to the field angle measured from the [001] axis and the magnetization normalized by its maximum value. The blue, green, and red lines correspond to the fields of 10 T, 20 T, and 30 T, respectively. The arrows indicate the crystallographic directions in each plot.

small magnetization. Importantly, the local minima in $M(\theta)$ are observed around $\theta = 0^\circ, 90^\circ, 180^\circ,$ and 270° as well as the local maxima around $\theta = 45^\circ, 135^\circ, 225^\circ,$ and 315° for $\mu_0H = 30$ T. These calculated results taking the CEF effect and the exchange interaction indicate that CeCoSi has additional hard and easy axes under high magnetic fields. Moreover, the additional axes also emerge when the magnetic field lies within the (110) plane, as shown in Fig. 7(b), indicating that the emergence is independent of the azimuth of the applied magnetic field. Since the sign reversal of magnetic torque occurs at the direction of easy and hard axes, this calculation is consistent with the observed fourfold symmetry in the magnetic torque. Note that our calculation shows that the easy axes lie slightly away from the field direction of $\theta = 45^\circ$, while the sign reversal of the magnetic torque appears at $\theta = 45^\circ$ within our experimental resolution.

TABLE II. CEF energy scheme and corresponding wave functions.

E (K)	$ -5/2\rangle$	$ -3/2\rangle$	$ -1/2\rangle$	$ 1/2\rangle$	$ 3/2\rangle$	$ 5/2\rangle$
163	0	0	1	0	0	0
163	0	0	0	1	0	0
122	0	0.325	0	0	0	0.945
122	0.945	0	0	0	0.325	0
0	0	-0.945	0	0	0	0.325
0	0.325	0	0	0	-0.945	0

C. CEF energy scheme

We calculate the energy diagram using the parameters shown in Table I. The CEF wave functions are given by [25,32]

$$|\Gamma_7^{\text{GS}}\rangle = \alpha|\pm 5/2\rangle - \beta|\mp 3/2\rangle, \quad (11)$$

$$|\Gamma_7^1\rangle = \beta|\pm 5/2\rangle + \alpha|\mp 3/2\rangle, \quad (12)$$

$$|\Gamma_6\rangle = |\pm 1/2\rangle, \quad (13)$$

where α and β are the linear coefficients satisfying $\alpha, \beta > 0$ and $\alpha^2 + \beta^2 = 1$, which are determined by the CEF parameters obtained in the previous section. The obtained CEF energy scheme and corresponding wave functions are listed in Table II. The energy diagram with the parameters in Table I yields $\Delta_1 = 122$ K and $\Delta_2 = 163$ K, where the energy diagram is denoted by two parameters of Δ_1 and Δ_2 as the energy from the Γ_7^{GS} ground state to Γ_7^1 and Γ_6 . The obtained energy diagram is consistent with that reported by the inelastic neutron scattering [31], although the present calculation may have an error of ~ 10 K.

V. DISCUSSIONS

A. Magnetic properties and CEF energy scheme

First, we discuss the concave feature of the magnetization curves observed around B_c . This feature is often observed in two-dimensional Heisenberg spin systems due to the spin fluctuation resulting from low dimensionality [52,53]. In CeCoSi, strong spin fluctuations can be anticipated because the energy scale of T_N is smaller than that of the Weiss temperature [20] and the exchange energy [31]. Such a strong fluctuation in CeCoSi might result in the concave magnetization curves.

In previous reports, the magnetic anisotropy of CeCoSi was considered to be quite small compared with other Ce compounds. However, our magnetic torque measurements have revealed the strong magnetic anisotropy under high magnetic fields as well as the emergence of the other hard axes, which are numerically reproduced. To discuss the origin of the unique magnetic anisotropy, we calculate the field dependence of the CEF energy levels, as presented in Fig. 8. The field dependence of the GS linearly shifts as a function of the magnetic fields below 20 T, while it gradually turns into nonlinear behavior above 20 T. This nonlinear behavior suggests the hybridization of the CEF wave functions between the GS and the excited states. Considering that the "was-waist" magnetic anisotropy occurs above 20 T, the fourfold magnetic anisotropy can reflect the mixing of the CEF wave functions.

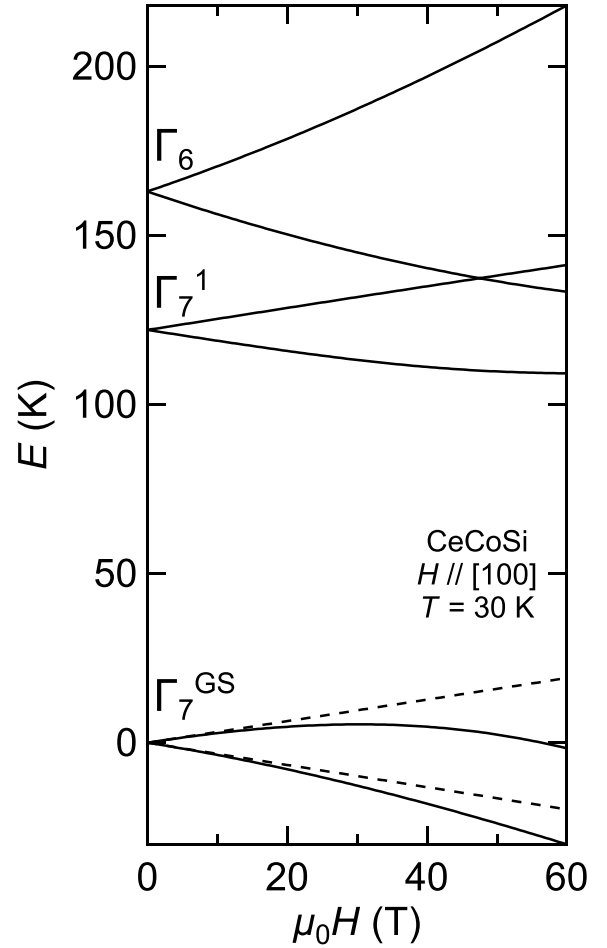


FIG. 8. Field dependencies of the CEF energy levels in CeCoSi for $H//[100]$. The dotted lines are the linear extrapolations from zero magnetic fields.

Although the hybridization becomes evident above 20 T in our calculation, the fourfold anisotropy is observed at 15 T in our torque measurements. This suggests that the influence of hybridization on the magnetic anisotropy starts from lower fields than estimated by our model. Such a hybridization increases multipole degrees of freedom and assists multipolar orderings as discussed in CeTe [54,55]. The origin of multipole degrees of freedom is still under debate in this compound; however, our results experimentally indicate that there is a hybridization of CEF wave functions despite the large CEF energy gaps of ~ 100 K. The hybridization must play a key role in multipole degrees of freedom in CeCoSi.

In addition to the fourfold magnetic anisotropy, we have observed the huge hysteresis for $H//[100]$ at 1.5 K. One possibility of this origin is that the field-induced transition at B_c has the character of a first-order phase transition. In fact, the theoretical work has pointed out that the order of the phase transition can change depending on the field direction [25]. If the transition is the first-order phase transition, there must be a point where the transition switches from first order to second order, because the transition is the second-order phase transition at zero magnetic field. However, no previous studies have reported the first-order nature of the phase transition so

far. Detailed high magnetic field experiments are needed to elucidate the order of the phase transition.

Next, we compare our experimental results with the recent theoretical study. Yatsushiro *et al.* theoretically comprehended the possible AFQ and AFQ + AFM orders for Phase II and Phase III, respectively [25]. Our experiments and calculation strongly indicate that the ground state is Γ_7^{GS} and the first excited state is Γ_7^1 . In this CEF energy scheme, $Q_{3z^2-r^2}$, Q_{zx} , and Q_{yz} type AFQ orders are theoretically allowed in Phase II. Here, the notations x , y , and z correspond to the crystallographic [100], [010], and [001] axes, and $r = \sqrt{x^2 + y^2 + z^2}$. Considering that the Ce $4f$ moments point to the [100] axis [31], the possible AFQ + AFM orders in Phase III are $Q_{zx} + M_x$ and $Q_{yz} + M_y$ according to their model. In the present experimental research, we have applied the magnetic fields along the [001] axis to Phase III and observed the phase transition to Phase II by magnetization, TDO, MCE, and specific heat measurements. However, the theoretical study pointed out that neither $Q_{zx} + M_x$ nor $Q_{yz} + M_y$ orders show the clear phase transition to Phase II for $H//[001]$. Therefore, there is a discrepancy between our experimental observations and the theoretical prediction, which indicates that the real system of CeCoSi is much more complicated than the model proposed by Yatsushiro *et al.*. The possible cause of this inconsistency is the triclinic lattice distortion in Phase II and III reported by the recent XRD experiments [27]. Such a structural change makes the symmetry around f electrons lower and affects the multipolar orderings. In addition, the recent NMR experiment proposed the ferro quadrupolar order below 10 T [29], which prompts further theoretical investigations taking the influence of the triclinic lattice distortion to unveil the OP of Phase II in CeCoSi.

B. Thermal properties and unconventional ordering

We discuss the origin of the large b in Phase II detected in the specific heat measurement. One possibility for the explanation is that the antiferromagnetic-like spin configuration remains above the critical fields, which can induce the three-dimensional magnon excitation as b . However, the magnetization in Phase II is close to the size of the calculated magnetic moment of Γ_7^{GS} . This suggests that almost all spins point along the field direction, in which the antiferromagnetic-like spin excitation is expected to follow an exponential behavior [56]. Such a behavior is not observed in the present study. Another possible origin is the lattice instability caused by $4f$ electrons. The powder XRD study under pressure pointed out the valence instability above 2 GPa and subsequent structural transition at 5 GPa in this compound [57,58]. Recent optical reflection measurement under ambient pressure also pointed out the electronic/valence instability around T_0 [59]. This instability can enhance the coefficient b . However, C_{lattice} is about 10^2 times smaller than C_{ano} and it is hard to consider that C_{lattice} plays a dominant role in increasing b .

Although the critical fluctuation around the critical field might affect the estimation of b , we propose the possibility that a Goldstone mode of “hidden order parameter” causes the T^3 temperature dependence in specific heat. Such a power-law

behavior in specific heat, including magnon excitations, derives from the energy dispersion relationship of a gapless mode. When the dispersion is linear in momentum space, the specific heat follows $C \propto T^d$, where d is the dimensionality of the dispersion. The power-law behavior of the specific heat and the dispersion relationship of the gapless mode have been studied in some systems. For example, the Goldstone mode in a spin-nematic state, which is a spin quadrupole ordered state discussed in a quantum spin system, has a linear dispersion and specific heat obeys the $C \propto T^d$ power law [39,60]. In the AFQ phase of CeB₆, the specific heat obeys T^3 power law [61] along with the linear dispersion observed in the inelastic neutron scattering experiment [62]. Although the dispersion relationship is still unclear in CeCoSi, the present observation of the T^3 temperature dependence might also be a result of a Goldstone mode of an unconventional order parameter, such as an electronic quadrupole moment.

VI. SUMMARY

We report the magnetic and thermal properties of CeCoSi under low temperatures and high magnetic fields, where a hidden ordered state is expected to appear. The angle dependence of Phase II-III boundary is determined by our magnetization, contactless resistivity, and MCE measurements. Along with the unusual angle dependence of the phase boundary, the unique fourfold anisotropy in the magnetic torque is revealed. The two-sublattice mean-field calculation is presented, which reproduces the experimental magnetization and magnetic susceptibility data. The magnetic anisotropy is calculated by taking the CEF effect and the exchange interaction into consideration, which explains the fourfold anisotropy. The CEF energy scheme is also deduced by the obtained CEF parameters. We present that the unique magnetic anisotropy is relevant to the hybridization of the CEF wave functions. The hybridization must be the origin of multipole degrees of freedom in CeCoSi. We compare our experimental results with the recent theoretical study. Our results are partly inconsistent with the theoretical predictions, which is probably because of the triclinic lattice distortions. The low-temperature C_p data show the enhancement of b in Phase II. Although its origin remains unclear, the enhancement of b could relate to the Goldstone mode of “hidden order parameter” in Phase II.

ACKNOWLEDGMENTS

We acknowledge fruitful discussions with Satoru Hayami, Yuki Yanagi, Takemi Yamada, Ryosuke Kurihara, Toshihiro Nomura, Shinya Uji, Takasada Shibauchi, Shinichiro Seki, Masashi Tokunaga, and Yasuyuki Kato. This work was supported by the Japan Society for the Promotion of Science (JSPS) Grants-in-Aid for 18H03683, 22H00104, and 22K13996. Y.K. acknowledges support from UTEC-UTokyo FSI Research Grant Program. T.K. was supported by a JSPS Research Fellowship and by JSPS KAKENHI Grant No. 23KJ0502. T.K. was also supported by Quantum Science and Technology Fellowship Program (Q-STEP).

- [1] J. A. Mydosh and P. M. Oppeneer, *Rev. Mod. Phys.* **83**, 1301 (2011).
- [2] J. A. Mydosh, P. M. Oppeneer, and P. S. Riseborough, *J. Phys.: Condens. Matter* **32**, 143002 (2020).
- [3] M. Takigawa, H. Yasuoka, T. Tanaka, and Y. Ishizawa, *J. Phys. Soc. Jpn.* **52**, 728 (1983).
- [4] K. Kubo and Y. Kuramoto, *J. Phys. Soc. Jpn.* **73**, 216 (2004).
- [5] A. S. Cameron, G. Friemel, and D. S. Inosov, *Rep. Prog. Phys.* **79**, 066502 (2016).
- [6] T. Tayama, T. Sakakibara, K. Kitami, M. Yokoyama, K. Tenya, H. Amitsuka, D. Aoki, Y. Onuki, and Z. Kletowski, *J. Phys. Soc. Jpn.* **70**, 248 (2001).
- [7] Y. Sato, H. Morodomi, K. Ienaga, Y. Inagaki, T. Kawae, H. S. Suzuki, and T. Onimaru, *J. Phys. Soc. Jpn.* **79**, 093708 (2010).
- [8] K. Kubo and T. Hotta, *Phys. Rev. B* **95**, 054425 (2017).
- [9] I. Ishii, H. Muneshige, Y. Suetomi, T. K. Fujita, T. Onimaru, K. T. Matsumoto, T. Takabatake, K. Araki, M. Akatsu, Y. Nemoto *et al.*, *J. Phys. Soc. Jpn.* **80**, 093601 (2011).
- [10] T. Onimaru, K. T. Matsumoto, Y. F. Inoue, K. Umeo, T. Sakakibara, Y. Karaki, M. Kubota, and T. Takabatake, *Phys. Rev. Lett.* **106**, 177001 (2011).
- [11] T. Onimaru, N. Nagasawa, K. T. Matsumoto, K. Wakiya, K. Umeo, S. Kittaka, T. Sakakibara, Y. Matsushita, and T. Takabatake, *Phys. Rev. B* **86**, 184426 (2012).
- [12] I. Ishii, H. Muneshige, S. Kamikawa, T. K. Fujita, T. Onimaru, N. Nagasawa, T. Takabatake, T. Suzuki, G. Ano, M. Akatsu, Y. Nemoto, and T. Goto, *Phys. Rev. B* **87**, 205106 (2013).
- [13] T. J. Sato, S. Ibuka, Y. Nambu, T. Yamazaki, T. Hong, A. Sakai, and S. Nakatsuji, *Phys. Rev. B* **86**, 184419 (2012).
- [14] K. Matsubayashi, T. Tanaka, A. Sakai, S. Nakatsuji, Y. Kubo, and Y. Uwatoko, *Phys. Rev. Lett.* **109**, 187004 (2012).
- [15] T. Taniguchi, M. Yoshida, H. Takeda, M. Takigawa, M. Tsujimoto, A. Sakai, Y. Matsumoto, and S. Nakatsuji, *J. Phys. Soc. Jpn.* **85**, 113703 (2016).
- [16] S. Hayami, H. Kusunose, and Y. Motome, *Phys. Rev. B* **90**, 024432 (2014).
- [17] S. Hayami, H. Kusunose, and Y. Motome, *J. Phys. Soc. Jpn.* **85**, 053705 (2016).
- [18] S. Hayami, M. Yatsushiro, Y. Yanagi, and H. Kusunose, *Phys. Rev. B* **98**, 165110 (2018).
- [19] H. Saito, K. Uenishi, N. Miura, C. Tabata, H. Hidaka, T. Yanagisawa, and H. Amitsuka, *J. Phys. Soc. Jpn.* **87**, 033702 (2018).
- [20] H. Tanida, K. Mitsumoto, Y. Muro, T. Fukuhara, Y. Kawamura, A. Kondo, K. Kindo, Y. Matsumoto, T. Namiki, T. Kuwai, and T. Matsumura, *J. Phys. Soc. Jpn.* **88**, 054716 (2019).
- [21] E. Lengyel, M. Nicklas, N. Caroca-Canales, and C. Geibel, *Phys. Rev. B* **88**, 155137 (2013).
- [22] H. Tanida, Y. Muro, and T. Matsumura, *J. Phys. Soc. Jpn.* **87**, 023705 (2018).
- [23] M. Yatsushiro and S. Hayami, *J. Phys. Soc. Jpn.* **89**, 013703 (2020).
- [24] M. Yatsushiro and S. Hayami, *Phys. Rev. B* **102**, 195147 (2020).
- [25] M. Yatsushiro and S. Hayami, *J. Phys. Soc. Jpn.* **91**, 104701 (2022).
- [26] M. Manago, H. Kotegawa, H. Tou, H. Harima, and H. Tanida, *J. Phys. Soc. Jpn.* **90**, 023702 (2021).
- [27] T. Matsumura, S. Kishida, M. Tsukagoshi, Y. Kawamura, H. Nakao, and H. Tanida, *J. Phys. Soc. Jpn.* **91**, 064704 (2022).
- [28] H. Hidaka, S. Yanagiya, E. Hayasaka, Y. Kaneko, T. Yanagisawa, H. Tanida, and H. Amitsuka, *J. Phys. Soc. Jpn.* **91**, 094701 (2022).
- [29] M. Manago, A. Ishigaki, H. Tou, H. Harima, H. Tanida, and H. Kotegawa, *Phys. Rev. B* **108**, 085118 (2023).
- [30] K. Mitsumoto, K. Tanaka, and H. Tanida, Fr-a-32, in *Int. Conf. Strongly Correlated Electron Systems 2019* (2019).
- [31] S. E. Nikitin, D. G. Franco, J. Kwon, R. Bewley, A. Podlesnyak, A. Hoser, M. M. Koza, C. Geibel, and O. Stockert, *Phys. Rev. B* **101**, 214426 (2020).
- [32] A. Thamizhavel, T. Takeuchi, T. D. Matsuda, Y. Haga, K. Sugiyama, R. Settai, and Y. Ōnuki, *J. Phys. Soc. Jpn.* **74**, 1858 (2005).
- [33] M. Méasson, H. Muranaka, T. Kawai, Y. Ota, K. Sugiyama, M. Hagiwara, K. Kindo, T. Takeuchi, K. Shimizu *et al.*, *J. Phys. Soc. Jpn.* **78**, 124713 (2009).
- [34] I. Sugitani, Y. Okuda, H. Shishido, T. Yamada, A. Thamizhavel, E. Yamamoto, T. D. Matsuda, Y. Haga, T. Takeuchi, R. Settai, and Y. Ōnuki, *J. Phys. Soc. Jpn.* **75**, 043703 (2006).
- [35] A. Kondo, K. Kindo, K. Kunimori, H. Nohara, H. Tanida, M. Sera, R. Kobayashi, T. Nishioka, and M. Matsumura, *J. Phys. Soc. Jpn.* **82**, 054709 (2013).
- [36] H. Tanida, M. Nakamura, M. Sera, T. Nishioka, and M. Matsumura, *Phys. Rev. B* **92**, 235154 (2015).
- [37] E. Ohmichi and T. Osada, *Rev. Sci. Instrum.* **73**, 3022 (2002).
- [38] T. Coffey, Z. Bayindir, J. F. Decarolis, M. Bennett, G. Esper, and C. C. Agosta, *Rev. Sci. Instrum.* **71**, 4600 (2000).
- [39] Y. Kohama, H. Ishikawa, A. Matsuo, K. Kindo, N. Shannon, and Z. Hiroi, *Proc. Natl. Acad. Sci. USA* **116**, 10686 (2019).
- [40] L. Jiao, M. Smidman, Y. Kohama, Z. S. Wang, D. Graf, Z. F. Weng, Y. J. Zhang, A. Matsuo, E. D. Bauer, H. Lee, S. Kirchner, J. Singleton, K. Kindo, J. Wosnitza, F. Steglich, J. D. Thompson, and H. Q. Yuan, *Phys. Rev. B* **99**, 045127 (2019).
- [41] Y. Kohama and K. Kindo, *Rev. Sci. Instrum.* **86**, 104701 (2015).
- [42] S. Imajo, C. Dong, A. Matsuo, K. Kindo, and Y. Kohama, *Rev. Sci. Instrum.* **92**, 043901 (2021).
- [43] R. C. Sherwood, J. P. Remeika, and H. J. Williams, *J. Appl. Phys.* **30**, 217 (1959).
- [44] C. Kuroda, T. Miyadai, A. Naemura, N. Niizeki, and H. Takata, *Phys. Rev.* **122**, 446 (1961).
- [45] I. Yamamoto, *J. Phys. Soc. Jpn.* **45**, 1545 (1978).
- [46] K. Tokuhara, Y. Ohtsu, F. Ono, O. Yamada, M. Sagawa, and Y. Matsuura, *Solid State Commun.* **56**, 333 (1985).
- [47] T. Ishida, K. Okuda, H. Asaoka, Y. Kazumata, K. Noda, and H. Takei, *Phys. Rev. B* **56**, 11897 (1997).
- [48] S. Kumar, C. E. Patrick, R. S. Edwards, G. Balakrishnan, M. R. Lees, and J. B. Staunton, *J. Phys.: Condens. Matter* **32**, 255802 (2020).
- [49] Y. Kohama, K. Mochizuki, T. Terashima, A. Miyata, A. DeMuer, T. Klein, C. Marcenat, Z. L. Dun, H. Zhou, G. Li, L. Balicas, N. Abe, Y. H. Matsuda, S. Takeyama, A. Matsuo, and K. Kindo, *Phys. Rev. B* **90**, 060408(R) (2014).
- [50] C. D. Bredl, F. Steglich, and K. D. Schotte, *Z. Phys. B* **29**, 327 (1978).
- [51] M. T. Hutchings, *Solid State Phys.* **16**, 227 (1965).
- [52] P. A. Goddard, J. Singleton, P. Sengupta, R. D. McDonald, T. Lancaster, S. J. Blundell, F. L. Pratt, S. Cox, N. Harrison, J. L. Manson, H. I. Southerland, and J. A. Schlueter, *New J. Phys.* **10**, 083025 (2008).

- [53] H. Kikuchi, K. Kunieda, T. Asano, Y. Fujii, Y. Inagaki, A. Matsuo, and K. Kindo, *Phys. Procedia* **75**, 653 (2015).
- [54] Y. Kawarasaki, T. Matsumura, M. Sera, and A. Ochiai, *J. Phys. Soc. Jpn.* **80**, 023713 (2011).
- [55] H. Takaguchi, Y. Hayashi, T. Matsumura, K. Umeo, M. Sera, and A. Ochiai, *J. Phys. Soc. Jpn.* **84**, 044708 (2015).
- [56] A. U. B. Wolter, L. T. Corredor, L. Janssen, K. Nenkov, S. Schönecker, S.-H. Do, K.-Y. Choi, R. Albrecht, J. Hunger, T. Doert, M. Vojta, and B. Büchner, *Phys. Rev. B* **96**, 041405(R) (2017).
- [57] Y. Kawamura, H. Tanida, R. Ueda, J. Hayashi, K. Takeda, and C. Sekine, *J. Phys. Soc. Jpn.* **89**, 054702 (2020).
- [58] Y. Kawamura, K. Ikeda, A. N. B. A. Dalan, J. Hayashi, K. Takeda, C. Sekine, T. Matsumura, J. Gouchi, Y. Uwatoko, T. Tomita *et al.*, *J. Phys. Soc. Jpn.* **91**, 064714 (2022).
- [59] S. I. Kimura, H. Watanabe, S. Tatsukawa, and H. Tanida, *J. Phys. Soc. Jpn.* **92**, 043704 (2023).
- [60] A. Smerald and N. Shannon, *Phys. Rev. B* **88**, 184430 (2013).
- [61] T. Müller, W. Joss, J. V. van Ruitenbeek, U. Welp, P. Wyder, and Z. Fisk, *J. Magn. Magn. Mater.* **76-77**, 35 (1988).
- [62] L. P. Regnault, W. A. C. Erkelens, J. Rossat-Mignod, C. Vettier, S. Kunii, and T. Kasuya, *J. Magn. Magn. Mater.* **76-77**, 413 (1988).